Energy & Environmental Science

ROYAL SOCIETY OF CHEMISTRY

PAPER

View Article Online
View Journal

Cite this: DOI: 10.1039/d5ee07740k

Transient interference-based spectroscopy for a molecular-bond-sensitive probe of lithium ion batteries

Mengyun Hu,†[abc] Enlai Wan,†[ac] Yu Qiao,[abc] Shupeng Xu,[abc] Shiwen Li,[ac] Rui Zhu,[ac] Jiamin Guo,[ac] Xihao Chen [d] and Heping Zeng †*[abc]

Received 22nd December 2025,
Accepted 30th March 2026

DOI: 10.1039/d5ee07740k

rsc.li/ees

The lack of effective methods to track *in situ* lithium-ion distribution and structural evolution remains a bottleneck in the battery industry, yet no techniques currently allow *in situ* dynamic detection of detrimental Li_2O under realistic conditions. Here, a molecular-bond-sensitive probe technique is developed by leveraging transient interference-based spectroscopy (TIBS). By creating structured plasma channels through nonlinear interference of multiple femtosecond laser filaments, we achieve extreme spatial confinement of laser pulses, enabling peak intensities above 10^{14} W cm^{-2}. This field directly ruptures molecular bonds through tunneling ionization and triggers Coulomb explosion, disintegrating materials into constituent elements and fragments while preserving molecular signature information. The resulting element-specific emissions allow intrinsic probing of the original chemical states and local environments. When coupled with machine learning algorithms, this technique enables precise identification of lithium concentration changes as low as 0.3%, making it particularly valuable for *in situ* monitoring of atomic-scale structural changes and distinguishing the Li_2O side product from active materials.

Broader context

Advancing next-generation batteries with higher energy density and longer lifespan is critical for the widespread electrification of transportation and grid-scale renewable energy storage. A fundamental obstacle in this pursuit is the inability to directly observe, in real time and under operating conditions, the intricate internal dynamics—such as lithium-ion migration and the formation of detrimental side products like Li_2O—that ultimately govern battery performance and degradation. This lack of effective *in operando* diagnostics at the molecular level hinders the rational design of new materials and the optimization of device engineering. Here, we develop a novel molecular-bond-sensitive probe technique that overcomes this barrier. By enabling the precise, dynamic tracking of lithium distribution and the unambiguous identification of Li_2O formation at the atomic scale, our method provides an unprecedented window into the "black box" of battery operation. This breakthrough not only offers a direct path to deconvolute complex degradation mechanisms but also establishes a generalizable platform for probing ultrafast chemical and structural evolution in a vast array of materials beyond energy storage, from catalysts to semiconductors.

Introduction

The accelerating global transition towards carbon neutrality has positioned lithium-ion battery technology as a cornerstone of the future energy landscape,[1–3] driving a profound transformation in energy utilization.[4–7] Its applications have expanded beyond consumer electronics and electric vehicles to critical sectors such as aerospace and grid-scale energy storage.[8–11] The overall performance and safety of a lithium-ion battery system are primarily dictated by the electrode material, including its chemical composition, crystal structure, surface morphology, and elemental distribution.[12–14] However, we still lack *in situ* probes to track the microscopic movement and spatial distribution of lithium ions, or to capture the dynamic structural evolution of electrode materials, such as phase transitions and lattice rearrangements during lithium (de)intercalation. The continuous generation of Li_2O permanently sequesters active lithium and electrolyte components, leading directly to irreversible capacity loss. To date, no

[a] State Key Laboratory of Precision Spectroscopy, and Hainan Institute, East China Normal University, Shanghai 200062, China. E-mail: hpzeng@phy.ecnu.edu.cn
[b] Chongqing Key Laboratory of Precision Optics, Chongqing Institute of East China Normal University, Chongqing 401120, China
[c] Institute of Precision Optical Equipment for Marine Surveys (POEMS), Yazhou Bay Science and Technology City, Sanya 572000, Hainan, China
[d] School of Materials Science and Engineering, Chongqing University of Arts and Sciences, Chongqing 402160, China
† These authors contributed equally.

techniques are able to effectively monitor Li_2O nucleation, growth, distribution, or decomposition. Current mainstream analytical techniques for battery electrodes, such as X-ray diffraction,[15] scanning electron microscopy,[16] transmission electron microscopy,[17] X-ray photoelectron spectroscopy,[18] and Auger electron spectroscopy,[19] face challenges in accurately capturing the distribution of light elements like lithium or tracking multi-scale structural evolution. These methods involve destructive sampling and complicated preparation procedures, rendering them unsuitable for industrial applications.

While laser-induced breakdown spectroscopy (LIBS) has been widely used for elemental analysis and depth profiling in battery materials, it faces fundamental limitations in molecular-level characterization. Conventional laser ablation requires microsecond-scale plasma cooling periods, resulting in the loss of molecular bond specificity. Furthermore, its analytical sensitivity and quantitative accuracy are severely compromised by complex electrode matrix effects, making it particularly challenging to distinguish critical chemical states such as Li_2O formation from active lithium compounds or to track elemental distribution with molecular signature preservation. Although femtosecond laser ablation could minimize plasma background fluorescence, the inherent plasma defocusing effect imposes a peak intensity limit of approximately 5×10^{13} W cm^{-2} in air—insufficient to significantly distort molecular potential barriers or induce observable bond breaking. The electron density in single filaments rarely exceeds 10^{17} cm^{-3},[20] falling short of the threshold required to initiate detectable avalanche ionization of battery materials.

To overcome these fundamental constraints, we have developed a multi-filament interference approach, termed Transient Interference-Based Spectroscopy (TIBS), that creates transient plasma grating structures. This configuration enables substantial enhancement of peak laser intensity and electron density, achieving the necessary conditions for efficient molecular bond breaking through tunnelling ionization and Coulomb explosion processes. The resulting spectral signatures maintain molecular-level specificity while providing the sensitivity required for precise material characterization, particularly in complex electrochemical systems where traditional methods prove inadequate. When integrated with spectral reconstruction and backpropagation artificial neural networks, the method achieves accurate identification of molecular bonds across different concentration ranges. This advancement represents a significant step forward in analytical spectroscopy, bridging the gap between conventional elemental analysis and intrinsic molecular-level detection capabilities.

Results and discussion

The TIBS approach employs nonlinear interference of three high-intensity femtosecond laser filaments to establish plasma grating channels. As illustrated in Fig. 1(a), during femtosecond laser propagation in air, a dynamic balance between Kerr self-focusing and plasma defocusing effects generates stable femtosecond filaments.[21] When two such filaments intersect, their interference creates periodic constructive fringes, where nonlinear self-focusing and plasma defocusing reach equilibrium at significantly enhanced peak intensities, forming a plasma grating[22] with a modulation period of $\lambda/[2\sin(\theta/2)]$, where λ represents the central laser wavelength of the femtosecond laser pulses and θ denotes the crossing angle between non-collinear filaments. In our experimental configuration with $\theta = 20^\circ$, this yields a plasma grating period of 2.3 μm, as shown in the photos in Fig. 1(a). Below the photo is the calculated spatial intensity distribution of the plasma channel. Notably, these plasma grating channels exhibit exceptional confinement characteristics with widths below 1 μm—significantly narrower than the ~100 μm diameter typical of single filaments in air—enabling tight self-guiding of laser pulses. The introduction of a third femtosecond filament creates a scaly plasma grating structure that further confines pulses within channels approximately 10 μm long and <1 μm wide. This extreme confinement elevates the peak laser intensity, exceeding 10^{14} W cm^{-2},[23] generating electric field strengths comparable to intramolecular fields. At these extreme field strengths, the laser–matter interaction proceeds through a cascade of ultrafast processes: initial tunneling ionization liberates electrons and ruptures molecular bonds; these freed electrons subsequently gain energy from the confined laser field, triggering avalanche ionization through collisions with atoms and molecular fragments. The resulting ensemble of highly charged positive ions after the instantaneous electron loss undergoes violent Coulomb repulsion—a Coulomb explosion—that disintegrates the molecular architecture into constituent species. In particular, these molecular species undergo repeated collisions with high-density electrons within the plasma grating channels, which initiate and sustain avalanche ionization for hundreds of nanoseconds post-irradiation, while their dynamic evolution preserves distinctive fingerprints of the original molecular structure. Different molecular bond excitations exhibit distinct characteristics and remain unaffected by matrix effects. Such laser-plasma synergistic excitations enable efficient molecular bond breaking and generate bond-sensitive spectra.

During the interaction between laser and materials, inelastic collisions dominate the excitation process. Tunnel ionization induced by extreme electric fields is a field-driven, non-collisional process. Electrons undergo reverse bremsstrahlung radiation and inelastic collisions with atoms and ions to obtain energy from the laser field and trigger avalanche ionization. During the plasma expansion stage, inelastic collisions mainly involve electron collision excitation, resulting in characteristic emission spectral lines.

TIBS technology possesses depth profiling capabilities. It has sufficient thickness resolution, enabling single-pulse measurement and allowing for layer-by-layer analysis. Under conditions of low laser energy and a limited number of pulses, the surface of the material can be detected. By adjusting the pulse energy and the number of pulses, under the excitation of multiple femtosecond pulses, each laser pulse ablates a thin and localized volume, rather than just the outermost layer of

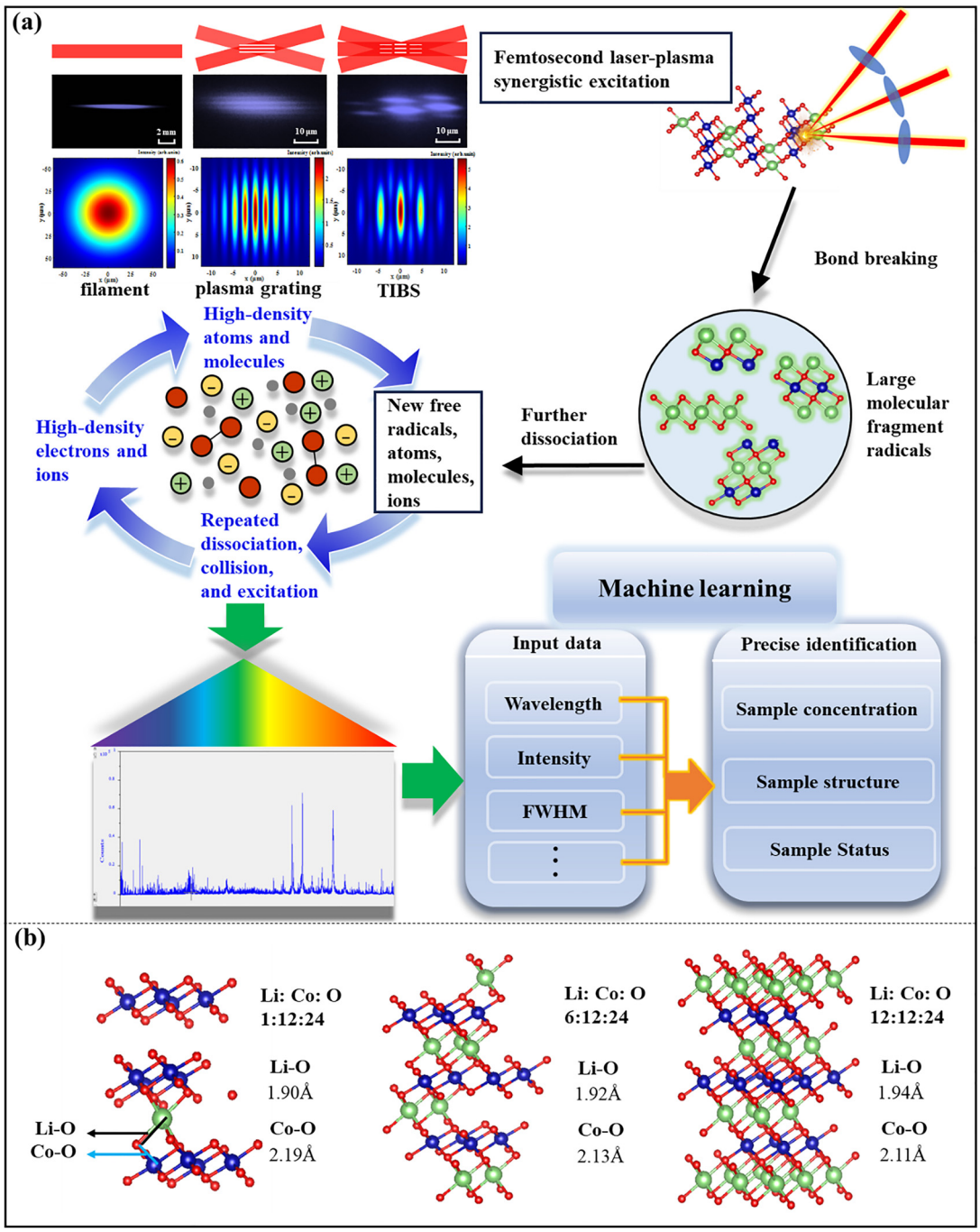

Fig. 1 (a) Schematic diagram, photos, and spatial intensity distribution of femtosecond filament, plasma grating, and TIBS. The photos and spatial intensity distribution map demonstrate that the width of the plasma channel is approximately 1 μm. Schematic diagram of chemical bond breaking induced by TIBS technology. (b) Structural changes in $LiCoO_2$ with different lithium concentrations. The crystal structures under three distinct atomic coordination environments are compared. Structural simulation gives the bond lengths for different lithium concentrations.

the material. This means that the signal collected by each pulse represents chemical information from a specific depth range, rather than just information from the outermost surface. By accumulating consecutive laser pulses, TIBS is able to detect from the electrode surface to the interior of the material, thus sequentially acquiring depth-resolved spectroscopic information. Therefore, TIBS technology enables the monitoring of compositional evolution along the thickness direction of the electrode, which is crucial for characterizing non-uniform delithiation and interfacial side reactions.

Considering the lithium-ion distribution characteristics of batteries during charging and discharging processes, we employed Vesta software to simulate structural changes in the $LiCoO_2$ cathode material at different lithium concentrations.[24]

As shown in Fig. 1(b), atomic-scale analysis reveals noticeable changes in Co–O and Li–O bond lengths with varying lithium-ion concentration. In $LiCoO_2$ cathode materials with different atomic ratios, the lengths of the Co–O bond are 1.90, 1.92, and 1.94 Å, and those of Li–O bond are 2.19, 2.13, and 2.11 Å, respectively. The specific atomic ratios are marked in Fig. 1(b). The results indicate that lithium-ion concentration directly influences the local bonding environment, inducing subtle adjustments in the electrode material structure. Therefore, developing high-precision quantitative analysis methods can facilitate the accurate identification of atomic-scale structural features and provide new pathways for highly sensitive diagnosis of battery states. TIBS technology, with its unique mechanism of breaking chemical bonds, is highly suitable for detecting differences in chemical bonds.

Lithium-ion battery technology utilizes various cathode material systems, with prominent examples including $LiFePO_4$, $LiCoO_2$, $LiMn_2O_4$, and $LiNiCoAlO_2$. We selected olivine-structured $LiFePO_4$ and layered $LiCoO_2$ as the representative cathode materials to assess TIBS performance for different chemical structures and elemental compositions. Intense femtosecond laser pulses were directed to interact with the electrode materials under ambient atmospheric conditions. Laser-induced emissions were analyzed using an on-chip integration mode of an ICCD camera (iStar, Andor Technology) integrated with a spectrometer (Mechelle 5000, Andor Technology). The transient dynamics of plasma evolution were resolved by varying the detection delay time while maintaining a fixed exposure duration of 0.2 seconds per acquisition. Each measurement accumulated 200 consecutive spectra to enhance the signal-to-noise ratio (SNR). TIBS technology does not require a specific gas environment. All measurements were performed in ambient air. Fig. 2(a) and (b) present the time-resolved spectra of $LiFePO_4$ and $LiCoO_2$, revealing distinct temporal characteristics in their plasma emission behavior. At zero delay time, the immediate laser–matter interaction, dominated by tunneling ionization and molecular bond rupture, produces the highest spectral line intensities. TIBS can generate atomic emissions from Li, Fe, and Co simultaneously—the process liberates all atomic species from the lattice in one explosive event, allowing for their simultaneous detection. Crucially, the absence of significant plasma background interference enables clear resolution of element-specific emissions—a notable advantage over nanosecond LIBS, where strong plasma fluorescence typically masks early-stage spectral features. As shown in Fig. 2(c) and (d), the temporal profiles of characteristic peak intensity and SNR reveal element-specific decay features. The Fe and Co spectral lines exhibit rapid decay, diminishing to near-background levels after 300 ns, while the Li signal remains detectable with up to 600 ns delay. These decays exhibit much longer equivalent lifetimes than the corresponding electronic emissions, indicating that these excited species experience significant impact excitations due to collision with high-density electrons in the plasma channels.

Across all delays, the Li signal exhibits consistently higher intensity than both Fe and Co. During laser interaction with both electrode materials, Li^+ ions are primarily ejected during Coulomb explosion, and their collision with electrons are enhanced within the plasma grating channels. Fe or Co ions were excited quite differently during the laser interaction period. In olivine-structured $LiFePO_4$, the Fe^{2+} ion has less tightly bound electrons compared to the Li^+ ion. The highly localized Fe–O bonds are broken first by the direct removal of electrons, and the Li–O bonds are broken during the resulting Coulomb explosion, while the covalently bonded phosphate framework behaves as a rigid disintegrating unit during Coulomb explosion. This was validated by the fact that negligible P emission lines were observed in $LiFePO_4$. In layered $LiCoO_2$, the laser field preferentially removes electrons from the cobalt and oxygen ions in the covalent-ionic network of the CoO_2 layer. The Co–O bonds are broken first by the direct removal of electrons, triggering a Coulomb explosion that dismantles the entire structure, including the ionic Li sites. All the excitations preserve the molecular bond signatures, whose characteristic features—including wavelength, intensity, line width, and temporal evolution—provide critical structural fingerprinting information for the electrode materials. An optimal acquisition delay was set at 300 ns for $LiFePO_4$ and 200 ns for $LiCoO_2$, providing maximum sensitivity for their respective elemental signatures while maintaining excellent spectral quality for discrimination of different material states.

The spectral performance was compared for three different excitation methods: single femtosecond filaments, plasma gratings, and the TIBS configuration. As demonstrated by the characteristic Li I 610.4 nm emission line shown in Fig. 2(e) and (f), the spectral intensities obtained through these three approaches show remarkable differences. The TIBS technique yields the strongest spectral signal, with intensity approximately four times greater than that achieved with single-filament excitation and about double that obtained through plasma-grating excitation. This confirms that TIBS plasma grating channels had enhanced laser electric fields and elevated electron density, thus giving the strongest molecular rupture and explosion for precise differentiation of material compositions across diverse concentration ranges, structural configurations, and chemical states.

As shown in Fig. 3(a) and (b), $LiFePO_4$ and $LiCoO_2$ dominate, with Li, Fe, and Co characteristic peaks.[25–27] As the electrode materials are coated onto an aluminum foil substrate, characteristic aluminum signals are detected in both spectra. It is noteworthy that TIBS provides powerful bond-breaking specificity to distinguish the detrimental side product Li_2O[28–30] from other active lithium compounds. Fig. 3(c–f) present spectra obtained under the TIBS configuration for the mixture of $LiFePO_4$ and $LiCoO_2$, and for Li_2O, Fe_2O_3, and CoO, respectively. The bond-sensitive nature of TIBS was evidenced by the strong Li I emission lines at 460.3 and 497.2 nm from Li_2O, which were much stronger than those from $LiFePO_4$ and $LiCoO_2$. The bond rupture in Li_2O is initiated by the direct ionization of the oxygen anion, leading to an instantaneous Coulomb explosion that violently disassembles Li_2O into its atomic ions, allowing for precise detection and differentiation

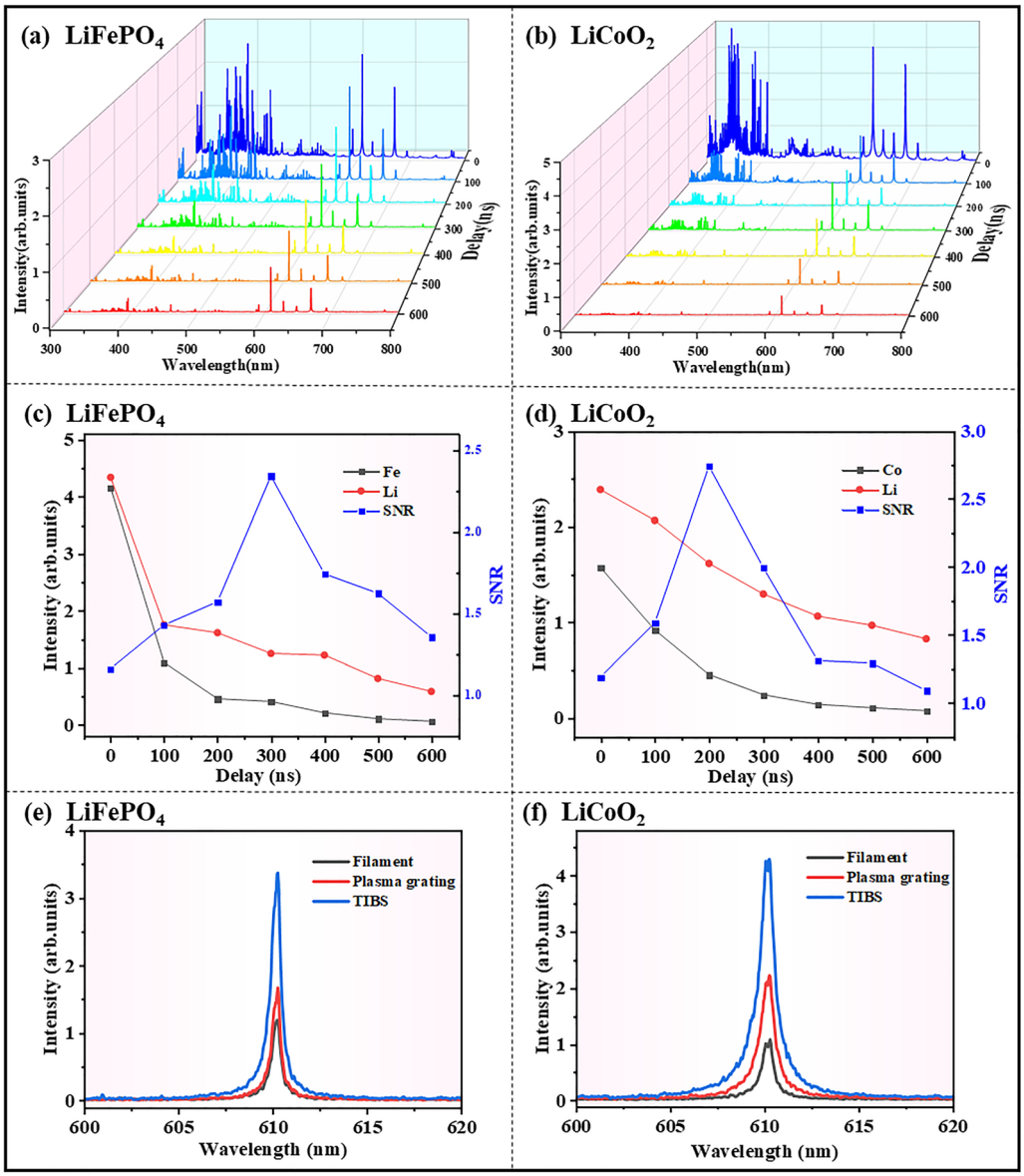

Fig. 2 Time evolution of spectra of (a) $LiFePO_4$ and (b) $LiCoO_2$. Their time-resolved spectra give the temporal evolution characteristics of plasma. Temporal variations in characteristic peak intensity and signal-to-noise ratio of (c) $LiFePO_4$ and (d) $LiCoO_2$. The different decay features of Li, Fe, and Co spectral lines reveal their distinct excitation modes. Spectra comparison of (e) $LiFePO_4$ and (f) $LiCoO_2$ achieved by three different excitation methods: single filament, plasma grating, and TIBS, respectively. TIBS obtains the strongest spectral signal, which confirms that the TIBS plasma channel enhances the laser electric field and increases the electron density.

from other lithium compounds, which, as aforementioned, undergo quite different bond rupture and Coulomb explosion.

As a battery electrode comprises composite materials, such as a blend of $LiFePO_4$ or $LiCoO_2$, conductive carbon, and a binder, the illuminating intense femtosecond laser pulse interacts with all components, and those with lower ionization thresholds or more localized electrons ionize more readily. Each distinct chemical phase in the mixture undergoes its own localized Coulomb explosion. In the TIBS configuration, intensified bond rupture and compound-specific Coulomb explosions produce observable atomic and molecular fragments of each individual component, which are ejected into plasma grating channels of enhanced electron density, resulting in dramatic enhancement of impact excitation, emitting a composite spectrum that contains quantifiable information about each component. When a composite battery electrode is subjected to an intense femtosecond laser pulse, as shown in Fig. 3(c), elemental signals for Li, Co, and Fe are detected simultaneously. The corresponding oxides show characteristic peaks identical to those in the electrodes, indicating that mechanical mixing and high-energy ball milling—key precursor processing steps in electrode material synthesis—could partially replicate the physicochemical properties of electrode materials, resulting in spectral consistency.

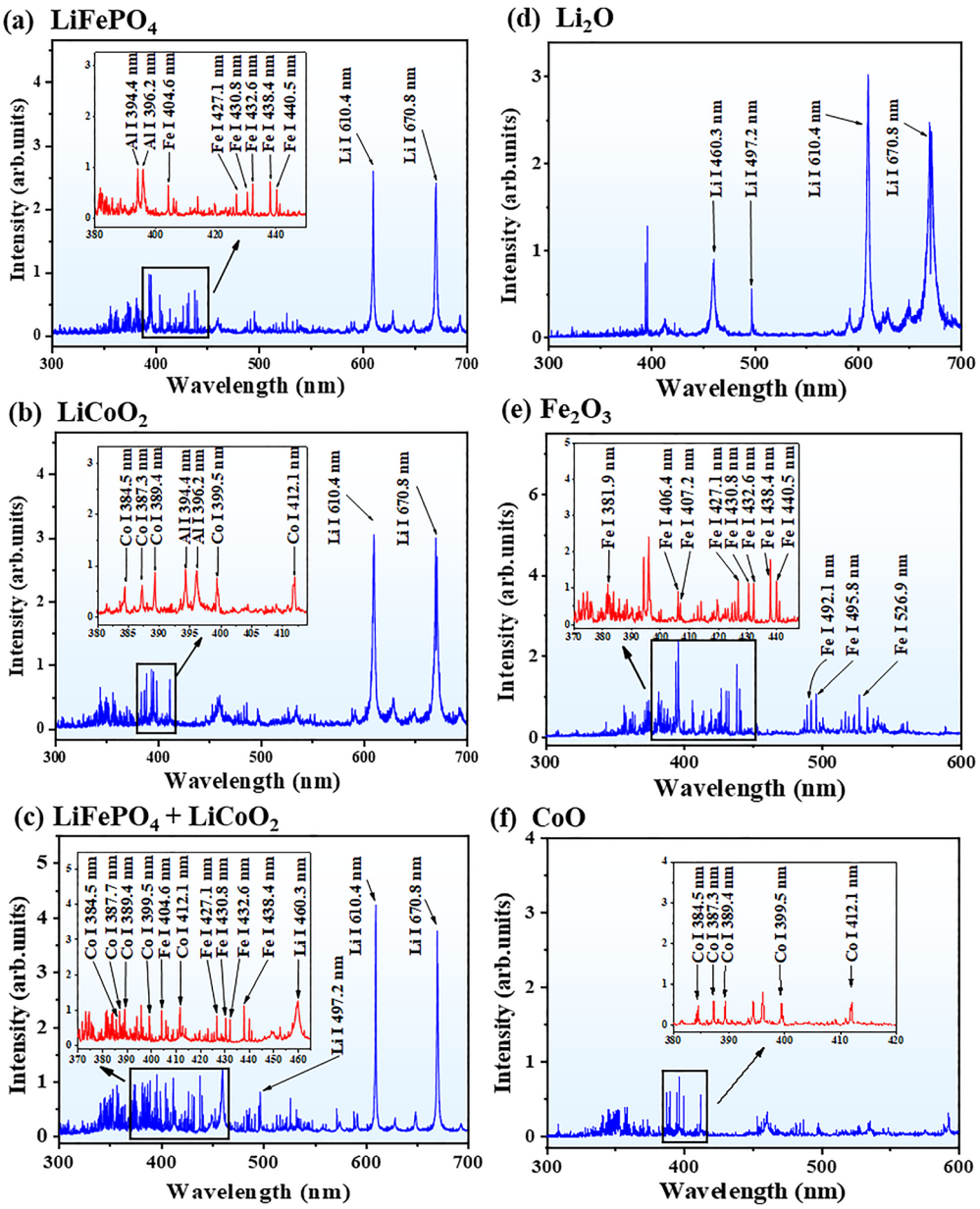

Fig. 3 TIBS spectra of (a) $LiFePO_4$, (b) $LiCoO_2$, and (c) mixture of $LiFePO_4$ and $LiCoO_2$, (d) Li_2O, (e) Fe_2O_3, and (f) CoO. In the spectrum, the characteristic peaks of Li, Fe, and Co are dominant. Aluminum is detected because the electrode materials are coated onto an aluminum foil substrate. Especially, in the spectrum of Li_2O, the intensity of Li I at 460.3 and 497.2 nm is much stronger than that of $LiFePO_4$ and $LiCoO_2$, which proves the bond-sensitive nature of TIBS.

Subsequently, guided by the ion migration behavior during the charging and discharging process, we conducted a quantitative analysis of the lithium battery electrode materials. First, we analyzed standard pellet samples of Li_2O, Fe_2O_3, and CoO with different concentrations. For each concentration, ten sets of spectra were collected under identical conditions. The average spectral line intensity served as the quantitative basis for establishing calibration curves for Li, Fe, and Co, as shown in Fig. 4(a–c). Each calibration curve exhibits good linearity, with R^2 values of 0.98 (Li), 0.98 (Fe), and 0.96 (Co), respectively. To simulate the complex component environment of actual electrode materials, mixtures of $LiFePO_4$ and $LiCoO_2$ were used as detection targets. Samples of different concentrations were prepared through standardized sample preparation procedures. Across different concentrations, the corresponding structural differences were successfully captured, as shown in Fig. 4(d–f). The characteristic spectral lines for each element show discernible changes across different compositions. Using lithium as an example, the main peak positions for the three concentrations are 610.20, 610.08, and 610.19 nm, with full width at half-maximum (FWHM) values of 0.95, 0.94, and 0.60 nm, respectively. This indicates that the characteristic spectral lines are profoundly sensitive reporters of the local chemical and physical environment. There exists a very close

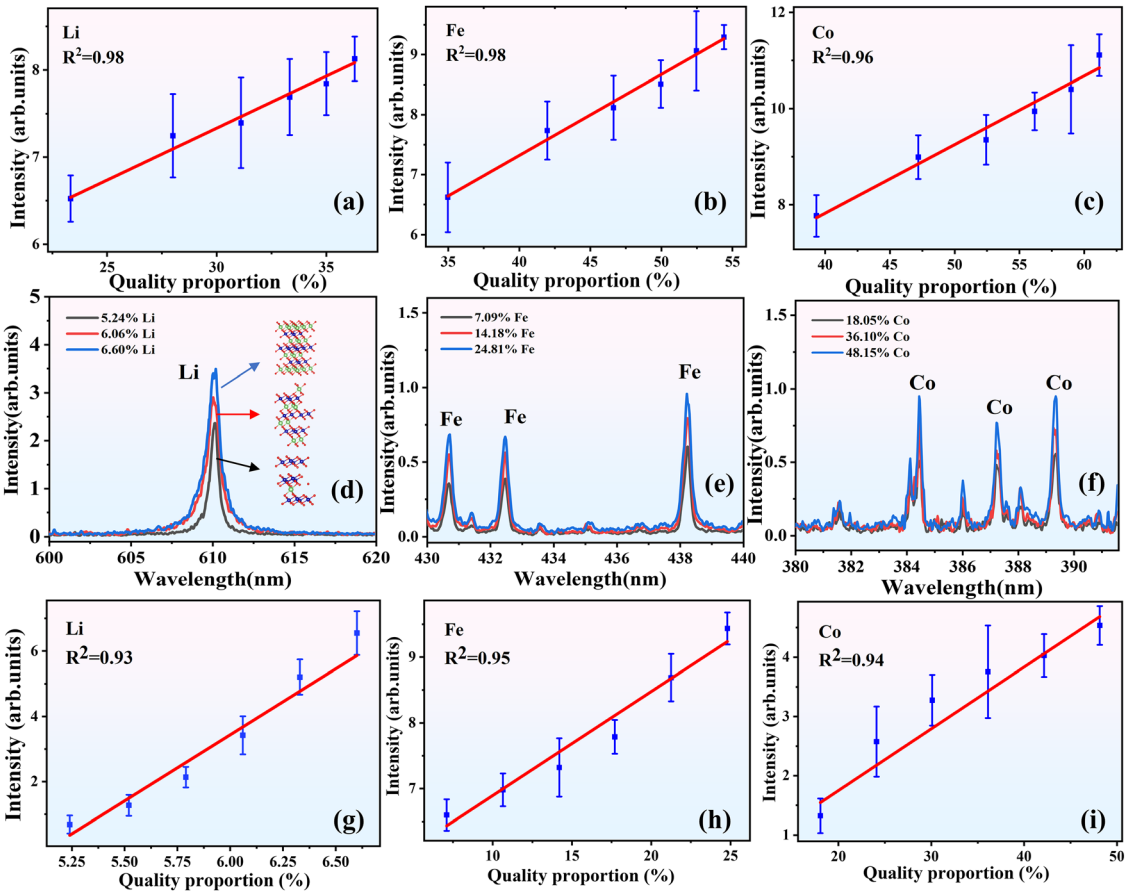

Fig. 4 Calibration curves of (a) Li, (b) Fe, and (c) Co in Li_2O, Fe_2O_3, and CoO. Ten sets of spectra were collected under the same conditions, and their average values were used as the quantitative basis. Characteristic spectra of (d) Li, (e) Co, and (f) Fe in the mixed electrode materials with a total mass of 0.2 g (0.14 g $LiFePO_4$ + 0.06 g $LiCoO_2$, 0.08 g $LiFePO_4$ + 0.12 g $LiCoO_2$, 0.04 g $LiFePO_4$ + 0.16 g $LiCoO_2$). Across different concentrations, corresponding structural differences were successfully captured, including spectral intensity, peak wavelength, linewidth, and spectral shape, which indicate that distinguishable spectral changes can be used to monitor atomic-scale structural differences. Calibration curves of (g) Li, (h) Fe, and (i) Co in two electrode material mixtures. Quality proportion means the ratio of the total mass of the target elements in the two materials to the total mass of 0.2 g.

correlation between spectral features and chemical structures, demonstrating that the discernible changes in spectral intensity, peak wavelength, line width, and spectral shape could be used to monitor atomic-scale structural differences.

Quantitative analysis was then performed on the mixed electrode materials. After standardized sample preparation *via* ball milling and pelletizing, calibration curves were established. As shown in Fig. 4(g–i), the spectral line intensities of Li, Fe, and Co maintain a good linear relationship with mass fractions, with R^2 values of 0.93 (Li), 0.95 (Fe), and 0.94 (Co), meeting quantitative analysis requirements, although the linearity is slightly inferior to that of the oxide standard samples. This difference primarily stems from the complex composition of the actual electrode materials: beyond the active materials $LiFePO_4$ and $LiCoO_2$, inactive components such as binders and conductive agents interfere with the plasma excitation process, affecting the quality of the calibration curves. Additionally, both sample types exhibit relatively large error ranges in their calibration curves.

The observed spectra contain discernible features, including spectral intensities, central wavelengths, and temporal evolutions, which reveal the physicochemical signatures of concentration, chemical states, and fragment dynamics, respectively. The entire rupture of the mixture, from the microscopic bond breaking and Coulomb explosion to the impact excitation in the macroscopic plasma grating structures, is encoded into the complex spectrum, which could be set as a high-dimensional fingerprinting pattern for machine-learning to decode the intrinsic molecular structure information.

The observed spectral lines were then processed by means of the so-called spectral reconstruction (SR) method.[31] This method establishes projection operations based on the intrinsic spectral characteristics, utilizing time-frequency features to map the observed data onto a low-dimensional feature subspace, thereby enhancing source feature identifiability while effectively suppressing noise. Using the highest concentration sample as the reference spectrum, spectral reconstruction was performed on the other five concentration samples. Fig. 5(a) compares the original and reconstructed spectra, showing significantly reduced background noise and more prominent signal features. When the reconstructed spectra were used for quantitative modeling, the resulting calibration curve exhibited

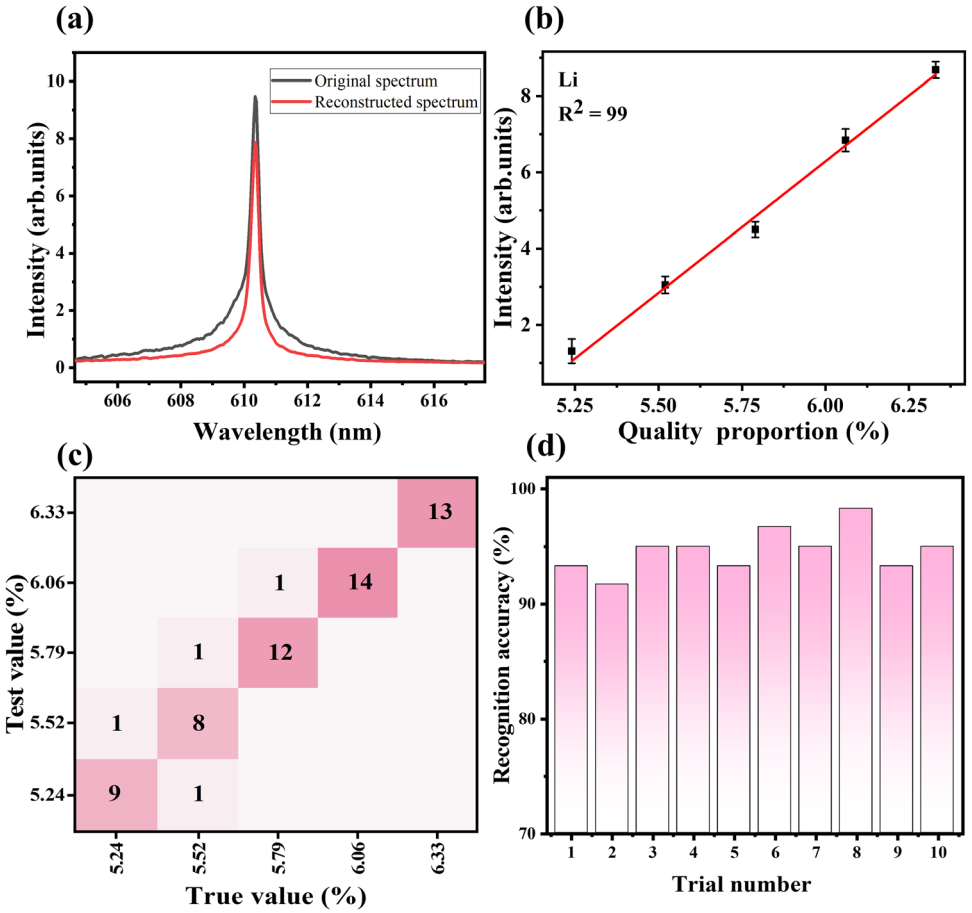

Fig. 5 (a) The difference between original spectrum and reconstructed spectrum. In the reconstructed spectrum, background noise is significantly reduced and signal features are more prominent. (b) Calibration curve of Li based on the reconstructed spectrum. The linearity of the calibration curve is significantly improved, and the error range is greatly reduced. (c) The confusion matrix of the test set. The deep purple squares indicate the correct number of identifications, totaling 56 groups. (d) Recognition accuracy of ten independent repeated experiments, with an average accuracy of approximately 94.7%.

markedly improved linearity, with the R^2 value increasing to 0.99, and the error margins were substantially narrowed, as shown in Fig. 5(b). Furthermore, based on the reconstructed spectral data, a backpropagation artificial neural network (BP-ANN) model was developed to identify electrode materials with different lithium concentrations. This model computes outputs through forward propagation and utilizes an error backpropagation mechanism with a gradient descent algorithm to iteratively adjust network weights and biases layer by layer, minimizing prediction error and achieving high-precision fitting of complex nonlinear mapping relationships. Given that lithium characteristic peaks vary in position, FWHM, and intensity across concentrations, the 604–617 nm wavelength range (comprising 362 data points), which encompasses the complete spectral profile, was selected as the input feature. The dataset includes five concentrations, with 40 spectra per concentration; 70% was allocated as the training set and 30% as the test set. The prediction results on the test set are shown in Fig. 5(c). If the test value is consistent with the true value, the recognition is correct, as shown in the dark purple square in the figure. The confusion matrix indicates that a total of 60 sets of data were used for validation, of which 56 were correctly identified and only four were incorrectly identified, yielding an identification accuracy of 93.3%. To assess model stability, ten independent replicate experiments were conducted, resulting in an average accuracy of approximately 94.7%, demonstrating good consistency, as shown in Fig. 5(d). TIBS reinforced by machine learning algorithms enables *in situ* and real-time monitoring of the microscopic chemical dynamics during the charging and discharging processes, capable of accurately detecting concentration changes as low as 0.3%. The successful recognition of different concentrations is equivalent to the identification of different bond lengths and atomic-scale structural differences.

The spectroscopic signature of the battery electrode is fundamentally determined by its local chemical environment and bonding, which could be mimicked through different processing routes. Specifically, mechanical mixing and high-energy ball milling could activate solid-state reactions of powder mixtures, such as Li_2O, Fe_2O_3, and CoO, to form compounds with requisite stoichiometries, mimicking chemical environments of a real complex electrode. Moreover, mechanical processing continually fractures particles and alters

the physicochemical states, creating surface defects or disordered states that can replicate the local bonding environments found in materials that have been cycled in a battery operation. These processing steps effectively create model systems that allow for more accurate machine learning model training.

Conclusions

In summary, we have demonstrated the bond-sensitive nature of TIBS that provides a powerful tool for state recognition and *in situ* performance monitoring of battery electrodes. Experimental results demonstrate that compared to femtosecond filament excitation, TIBS enhances the characteristic spectral line intensity by approximately fourfold while effectively suppressing background noise. Quantitative analysis of electrode samples with precisely controlled lithium content successfully captured spectral differences corresponding to distinct structures, indicating the method's capability to identify atomic-scale structural variations and validating the exceptional linear response and high-precision compositional analysis of TIBS for element identification. Further application of spectral reconstruction methods to process the original spectra improved the calibration curve fitting coefficient to 0.99 and significantly reduced error ranges. Integrated with machine learning algorithms, the approach achieved precise identification of concentration differences as low as 0.3%, with an identification accuracy of 94.7%. By integrating theoretical modeling, experimental diagnostics, and machine learning, this study proposes a rapid, high-precision comprehensive detection method for lithium battery electrode materials. This method not only enables quality and safety control of battery components but also facilitates rapid monitoring of lithium battery performance and identification of battery health status. Furthermore, it provides atomic-scale structural analysis capabilities, delivering key technical support for the development of next-generation energy storage systems.

TIBS technology is not only applicable to the Li_2O, $LiFePO_4$ and $LiCoO_2$ used here, but also usually applicable to various materials, including soft materials, organic components, polymers, *etc.* TIBS is a universal approach that can detect any element in principle. TIBS can analyze substances in almost all states (solid, gas, liquid). For batteries, it is very suitable for detecting various forms of samples such as thin films, thick electrodes, and powders (pressed into tablets), *etc.* The TIBS technique proposed in this work, with its unique bond-sensitive characteristics, is applicable to more complex cathode materials involving anionic redox reactions.

Methods

Experiment

The experimental setup is shown in Fig. 6. The light source used for laser ablation was a Ti:sapphire regenerative laser (Coherent Inc.) operated at a fundamental wavelength of 800 nm. It delivered 50 fs pulses at 1 kHz repetition rate, with a maximum single-pulse energy of 3 mJ. The laser beam first passed through two beam splitters to split into three beams of equal energy. Each beam passed through a focusing lens (f = 200 mm) to form a filament. Stepper motors were used to regulate the spatiotemporal synchronization of the three filaments. This ensured the formation of periodic plasma channels—plasma gratings. Unlike traditional pulsed lasers, this plasma grating was used to excite samples and generate plasma. The electrode material was fixed on an electric displacement platform, and excitation at different positions of the electrode material was achieved by adjusting the position of the displacement platform through a controller. The fluorescence emitted by the plasma was collected and focused onto an

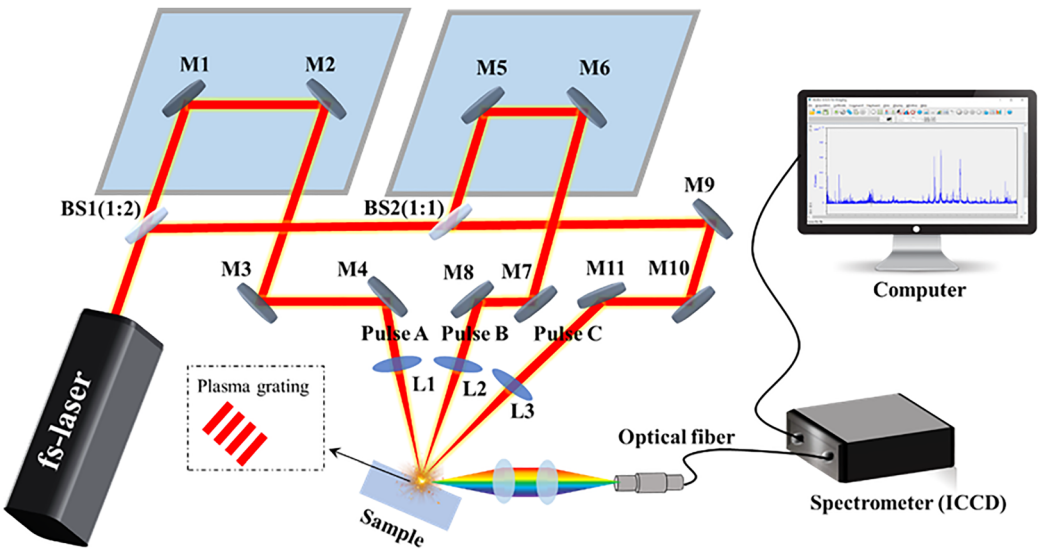

Fig. 6 TIBS experimental device. (A laser beam is divided into three beams of equal energy after passing through two beam splitters. After passing through several mirrors, they are focused to form three femtosecond filaments, which are adjusted to be spatially consistent and temporally synchronized. The three femtosecond filaments are nonlinearly coupled to form a plasma grating.)

optical fiber *via* two lenses (f = 30 mm), which was connected to an Echelle spectrometer (Mechelle 5000, Andor Technology). The spectrometer covered the spectral range of 200–850 nm with a resolution of 0.1 nm and was equipped with an intensified charge coupled device (ICCD) detector.

Differences in sample surface and volume do not affect the detection capability of TIBS. The minimum sample thickness required for reliable analysis of the current experimental setup can reach the micrometer level, and detecting thinner samples requires further optimization. There is no upper thickness limit, so long as the sampling space allows it. The area for signal extraction is controllable. In this experiment, the distance from the sample to the detection system is 12 mm. The signal is collected by two short-focus lenses (f = 30 mm) positioned at a 45° angle above the laser focal spot. The distance between the two lenses is twice the focal length, which can be adjusted as needed.

Sample preparations

When conducting quantitative analysis, Li_2O, Fe_2O_3, and CoO were initially used as the standard materials. These oxides were added to a 1.0 g standard soil matrix in increasing amounts: 1.0, 1.5, 2.0, 2.5, 3.0, and 3.5 g. The mass fractions of Li, Fe, and Co were then calculated for each concentration. After homogenizing the mixture through planetary ball milling, standardized tablets were prepared for TIBS analysis. Then, to simulate the complex characteristics of electrode materials in actual detection scenarios, mixed samples of $LiCoO_2$ and $LiFePO_4$ were prepared. Six sets of mixed samples with different mass ratios (total mass is 0.2 g) were designed. Standardized tablets were prepared using the same operating procedure for experimentation.

Spectral reconstruction method

This method comprises two main components: the establishment of a mapping matrix from standard spectra and the reconstruction of measured spectra based on this matrix. The mapping matrix is derived by projecting standard spectra onto a sinusoidal spectral basis. The mapping matrix $E_{m\times n}$ containing the positional transformation information is obtained by choosing the nearest ''neighbor'' rule from the set standard sine spectrum. The reconstructed spectrum $M'_{1\times m}$ in this method is calculated by:

$$R_{1\times n} = M_{1\times n}\cdot E_{m\times n} \quad (1)$$

$$M'_{1\times m} = R'_{1\times n}\cdot E^{T}_{m\times n} \quad (2)$$

where $M_{1\times m}$ is the measured spectrum, which is subjected to a mapping matrix to obtain the mapping spectrum $R_{1\times n}$. Then, the reconstructed sine spectrum $R'_{1\times n}$ is obtained after fitting the mapping spectrum $R_{1\times n}$. $M'_{1\times m}$ is the reconstructed spectrum obtained through the transpose matrix $E^{T}_{m\times n}$ of the mapping matrix $E_{m\times n}$.

Backpropagation artificial neural network

BP-ANN is a multi-layer feedforward network based on the gradient descent principle. It computes outputs through forward propagation and subsequently adjusts network parameters by backpropagating prediction errors. In classification tasks, input data undergo nonlinear transformations through hidden layers, ultimately generating class probability distributions at the output layer. During training, the system calculates error gradients by comparing predictions with ground-truth labels. These gradients are propagated backward through the network to iteratively update weights and biases, enabling the model to progressively approximate an optimal mapping relationship and achieve accurate classification. Here, given that lithium characteristic peaks vary in position, FWHM, and intensity across concentrations, the 604–617 nm wavelength range (comprising 362 data points), which encompasses the complete spectral profile, was selected as the input feature. By associating different spectral features with different battery states, high-precision state recognition of lithium batteries can be achieved.

Author contributions

M. Hu contributed to methodology, investigation, resources, project administration, supervision, and writing – review & editing. E. Wan contributed to methodology, investigation, visualization, and writing. Y. Qiao contributed to methodology, investigation, and resources. S. Xu contributed to methodology and investigation. S. Li contributed to methodology and investigation. R. Zhu contributed to methodology and investigation. J. Guo contributed to methodology. X. Chen contributed to methodology. H. Zeng contributed to methodology, investigation, funding acquisition, project administration, supervision, writing – original draft, and writing – review & editing. All authors discussed the results and reviewed the manuscript.

Conflicts of interest

All authors disclosed no financial/commercial conflict of interest.

Data availability

The data that support the findings of this study are available from the corresponding author upon reasonable request. Correspondence and requests for materials should be addressed to H. Zeng.

Acknowledgements

This work was supported by Quantum Science and Technology-National Science and Technology Major Project (2023ZD0301000); National Natural Science Foundation of China (12404360); Hainan Province Science and Technology Special Fund (ZDYF2025GXJS012); National Key Laboratory on Electromagnetic Environmental Effects and Electro-optical Engineering (No. JCKYS2024LD1); Chongqing Special Major Project for Technological Innovation and Application

Development (CSTB2025TIAD-STX0024); New Chongqing Youth Innovation Talent Program (CSTB2025YITP-QCRCX0029); Research Project of Shanghai Science and Technology Commission (22560730400).

Notes and references

1 E. Pomerantseva, *et al.*, Energy storage: The future enabled by nanomaterials, *Science*, 2019, **366**, eaan8285.
2 J. Q. He, *et al.*, Scalable production of high-performing woven lithium-ion fibre batteries, *Nature*, 2021, **597**, 57–63.
3 J. Xiao, *et al.*, From laboratory innovations to materials manufacturing for lithium-based batteries, *Nat. Energy*, 2023, **8**, 329–339.
4 Y. Chen, *et al.*, Advances in Lithium-Sulfur Batteries: From Academic Research to Commercial Viability, *Adv. Mater.*, 2021, **33**, 2003666.
5 G. Offer, *et al.*, Cool metric for lithium-ion batteries could spur progress, *Nature*, 2020, **582**, 485–487.
6 J. M. Turner, The matter of a clean energy future, *Science*, 2022, **376**, 1361.
7 C. Yuan, Sustainable battery manufacturing in the future, *Nat. Energy*, 2023, **8**, 1180–1181.
8 S. T. Han, *et al.*, Sequencing polymers to enable solid-state lithium batteries, *Nat. Mater.*, 2023, **22**, 1515–1522.
9 G. X. Lu, *et al.*, High-voltage electrosynthesis of organic–inorganic hybrid with ultrahigh fluorine content toward fast Li-ion transport, *Sci. Adv.*, 2023, **10**, eado7348.
10 S. Kalnaus, *et al.*, Solid-state batteries: The critical role of mechanics, *Science*, 2023, **381**, eabg5998.
11 Z. Y. Wang, *et al.*, Lithium anode interlayer design for all-solid-state lithium-metal batteries, *Nat. Energy*, 2024, **9**, 251–262.
12 S. Kim, *et al.*, A complex hydride lithium superionic conductor for high-energy-density all-solid-state lithium metal batteries, *Nat. Commun.*, 2019, **10**, 1081.
13 Y. N. Sun, *et al.*, Solvent co-intercalation in layered cathode active materials for sodium-ion batteries, *Nat. Mater.*, 2025, **24**(205), 1441–1449.
14 Y. N. Gao, *et al.*, Design lithium exchanged zeolite based multifunctional electrode additive for ultra-high loading electrode toward high energy density lithium metal battery, *Adv. Energy Mater.*, 2024, **15**, 231703.
15 D. W. Choi, *et al.*, Thermal stability and phase transformation of electrochemically charged/discharged $LiMnPO_4$ cathode for Li-ion batteries, *Energy Environ. Sci.*, 2011, **4**, 4560–4566.
16 K. J. Hayworth, *et al.*, Gas cluster ion beam SEM for imaging of large tissue samples with 10 nm isotropic resolution, *Nat. Methods*, 2020, **17**, 68–71.
17 Z. F. Huang, *et al.*, Grain rotation and lattice deformation during photoinduced chemical reactions revealed by in situ X-ray nanodiffraction, *Nat. Mater.*, 2015, **14**, 691–695.
18 G. Greczynski, *et al.*, X-ray photoelectron spectroscopy of thin films, *Nat. Rev. Methods Primers*, 2023, **3**, 40.
19 A. Hans, *et al.*, Experimental realization of Auger decay in the field of a positive elementary charge, *Phys. Rev. Lett.*, 2024, **132**, 203002.
20 S. Eisenmann, A. Pukhov and A. Zigler, Fine structure of a laser-plasma filament in air, *Phys. Rev. Lett.*, 2007, **98**, 155002.
21 J. H. Odhner, D. A. Romanov and R. J. Levis, Rovibrational wave-packet dispersion during femtosecond laser filamentation in air, *Phys. Rev. Lett.*, 2009, **103**, 075005.
22 M. Y. Hu, *et al.*, Plasma-grating-induced breakdown spectroscopy, *Adv. Photon.*, 2020, **2**, 065001.
23 A. Couairon and A. Mysyrowicz, Femtosecond filamentation in transparent media, *Phys. Rep.*, 2007, **441**, 47–189.
24 K. Momma and F. Izumi, VESTA 3 for three-dimensional visualization of crystal, volumetric and morphology data, *J. Appl. Crystallogr.*, 2011, **44**, 1272–1276.
25 S. Imashuku, *et al.*, Quantitative lithium mapping of lithium-ion battery cathode using laser- induced breakdown spectroscopy, *J. Power Sources*, 2018, **399**, 186–191.
26 L. Yang, *et al.*, The detection of elemental content changes in electrode coating using laser-induced breakdown spectroscopy, *Spectrochim. Acta, Part B*, 2024, **214**, 106896.
27 R. Pamu, *et al.*, Calibration-Free quantitative analysis of lithium-ion battery (LiB) electrode materials using laser-induced breakdown spectroscopy (LIBS), *ACS Appl. Energy Mater.*, 2021, **4**, 7259–7267.
28 T. C. Liu, *et al.*, In situ quantification of interphasial chemistry in Li-ion battery, *Nat. Nanotechnol.*, 2019, **14**, 50–56.
29 Z. A. Yu, Y. Cui and Z. N. Bao, Design principles of artificial solid electrolyte interphases for lithium-metal anodes, *Cell Rep. Phys. Sci.*, 2020, **1**, 100119.
30 M. Asadi, *et al.*, A lithium-oxygen battery with a long cycle life in an air-like atmosphere, *Nature*, 2018, **555**, 502–506.
31 R. Zhu, *et al.*, Ppb-Level ammonia sensor for exhaled breath diagnosis based on UV-DOAS combined with spectral reconstruction fitting neural network, *ACS Sens.*, 2024, **9**, 4286–4294.